

1 Development and application of a street-level meteorology and 2 pollutant tracking system (S-TRACK)

3 Huan Zhang^{1,2}, Sunling Gong^{1*}, Lei Zhang^{1*}, **Jingwei Ni²**, Jianjun He¹, Yaqiang Wang¹,
4 **Xu Wang³**, Lixin Shi², **Shi^{4,3}**, Jinyue Mo¹, Huabing Ke¹, Shuhua Lu¹

5 ¹ State Key Laboratory of Severe Weather & Key Laboratory of Atmospheric Chemistry of CMA, Chinese Academy of
6 Meteorological Sciences, Beijing 100081, China

7 ² Henan Tianlang Ecological Technology Co., Ltd., Zhengzhou 450000, China

8 ³ Hangzhou Yizhang Technology Co., Ltd., Hangzhou 310000, China

9 ^{3,4} Key Laboratory of Meteorology and Ecological Environment of Hebei Province, Shijiazhuang 050000, China

10 ³ Meteorological Institute of Hebei Province, Shijiazhuang 050000, China

11 Correspondence to: Sunling Gong (gongsl@cma.gov.cn) and Lei Zhang (leiz09@cma.gov.cn)

12 **Abstract.** A multi-model simulation system for street level circulation and pollutant
13 tracking (S-TRACK) has been developed by integrating the Weather Research and
14 Forecasting (WRF), the STAR-CCM+ (Computational Fluid Dynamics model - CFD) and
15 the Flexible Particle (FLEXPART) models. The winter wind environmental characteristics
16 and the ~~potential impact~~[potential contribution](#) of traffic sources on nearby receptor sites in
17 a city district of China are analysed with the system for January 2019. It is found that
18 complex building layouts change the structure of the wind field and thus have an impact
19 on the transport of pollutants. The wind speed inside the building block is smaller than the
20 background wind speed due to the dragging effect of dense buildings. Ventilation is better
21 when the dominant airflow is in the same direction as the building layout. Influenced by
22 the building layout, the local circulations show that the windward side of the building is
23 mostly the divergence zone and the leeward side is mostly the convergence zone, which is
24 more obvious for high buildings. With the hypothesis that the traffic sources are uniformly
25 distributed on each road and with identical traffic ~~volumes~~[intensity](#), the potential
26 contribution ratios ([PCR](#)) of four traffic sources to certain specific sites under the influence
27 of the street-level circulations are estimated with the method of residence time analysis. It

Formatted: Superscript

Formatted: Superscript

Formatted: Superscript

Formatted: Font: (Default) Times New Roman, (Asian) Times New Roman

Formatted: Superscript

Formatted: Font: (Asian) +Body Asian (宋体), (Asian) Chinese (China)

1 is found that the contribution ratio varies with the height of the receptor site. As a result of
2 the generally upward motion in the airflow, the position with the greatest [potential](#)
3 ~~contribution ratio~~[PCR](#) from the four road traffic sources is located on a certain height
4 [which is commonly influenced by the distance of this location from the traffic source and](#)
5 [the background wind field](#) (about 15m in this study). The potential contribution of a road
6 to one of the receptor sites is also investigated under different wind directions. The
7 established system and the results can be used to understand the characteristics of urban
8 wind environment and to help the air pollution control planning in urban areas.

9 **1. Introduction**

10 In recent decades, with the continuous development of urban construction in China,
11 urban environmental problems have become increasingly serious and attracted widespread
12 attentions. According to the 2019 China Ecological Environment Status Bulletin, 180 of
13 337 cities at the prefecture level exceeded ambient air quality standards. The complex
14 building layouts and differences in thermal structures within cities lead to extremely
15 complicated meteorological characteristics and pollutant transport in urban areas (Lei et
16 al., 2012; Fernando et al., 2010; Aynsley, 1989). Though the transport of atmospheric
17 pollution in urban areas is widely studied, the study on tracking the sources of pollutants
18 on the street-level is still lacking due to limitations in research methods.

19 Researches on the street-level atmospheric environment are mainly divided into three
20 methods: field measurements (Macdonald et al., 1997), laboratory simulation research
21 (Mavroidis et al., 2003), and model simulations (Steenburgh et al., 2015; Hendricks et al.,
22 2007; Yucong et al., 2014). The model simulation has become one of the main methods for

1 studying environmental problems at the street-level due to the easy control of simulation
2 conditions and simple processing steps. The Computational Fluid Dynamics (CFD) is a
3 numerical simulation method to study the fluid thermal-dynamic problems and is now
4 widely used in the studies related to microscale problems within the urban canopy
5 (Gosman, 1999). The core of CFD simulation method is to solve the Navier-Stokes
6 equations. Depending on the turbulence closure scheme, CFD ~~pre-processing~~ models can
7 be divided into three types: Direct numerical simulation (DNS), Reynolds-averaged
8 Navier–Stokes (RANS) (Liu et al., 2018;Zheng et al., 2015;Milliez and Carissimo, 2008))
9 and Large eddy simulation (LES) (Kurppa et al., 2018;Li et al., 2008;Sada and Sato, 2002).
10 The choice among the three methods depends on the costs and objectives. One of the most
11 important issues using CFD ~~simulation~~technology in the environment problems on the
12 street-level is to obtain accurate initial and boundary conditions (Ehrhard et al., 2000). To
13 solve this problem, the multi-scale coupling method is revealed as a good solution, which
14 uses the meteorological information from mesoscale model as the initial and boundary
15 conditions to drive CFD (Nelson et al., 2016). Tewari et al. (2010) proved that the CFD
16 simulation was improved significantly when the results of Weather Research and
17 Forecasting (WRF) model were used as the initial and boundary conditions. With the WRF
18 model, the community multiscale air quality (CMAQ) model, and the CFD (RANS)
19 approach, Kwak et al. (2015) built an urban air quality modelling system, which presented
20 a better performance than the WRF-CMAQ model in simulating nitrogen dioxide (NO₂)
21 and ozone (O₃) concentrations.

22 Nevertheless, the street-level air pollutant transport resulted from the nearby sources
23 was still not fully investigated. The Flexible Particle (FLEXPART) model (Stohl et al.,

1 2005;Stohl, 2003) is a gas-block trajectory-particle dispersion model based on the
2 Lagrangian particle method. The FLEXPART model can track the transport of tracers via
3 forward or backward simulation. Different from Eulerian model, the Lagrangian model is
4 not restricted by the Courant–Friedrichs–Lewy (CFL) condition (Stam, 1999) and thus, the
5 integration process in the Lagrangian model can be maintained with high spatial resolution
6 with acceptable computation efficiency. Initially, the FLEXPART model was driven by
7 global meteorological reanalysis data from [European Centre for Medium-Range Weather](#)
8 [Forecasts \(ECMWF\)](#) or [National Centers for Environmental Prediction \(NCEP\)](#). Fast and
9 Easter (2006) developed a FLEXPART version that used the WRF model output and was
10 optimized with technical level and output results. Nowadays, the WRF-FLEXPART model
11 has been widely used to research the regional transport of air pollutants (Yu et al., 2020;He
12 et al., 2020;Gao et al., 2020;He et al., 2017a;Brioude et al., 2013;de Foy et al., 2011). Cécé
13 et al. (2016) firstly applied the FLEXPART model at a small-scale resolution to analyse
14 potential sources of [nitrogen oxide \(NO_x\)](#) in urban areas, with the WRF-~~LES~~ model results
15 as the driving field. Though FLEXPART has been extensively applied in medium and
16 long-range transport cases (Madala et al., 2015;Heo et al., 2015;Sandeepan et al., 2013;Liu
17 et al., 2013), it has been rarely tested for street-level transport and small-scale resolution
18 grids.

19 The objective of the present work is to investigate the flow field characteristics and
20 ~~potential impact~~[potential contribution](#) of traffic sources to receptor sites, under real
21 building scenarios and meteorological conditions. To this end, a multi-model simulation
22 system for street level circulation and pollutant tracking (S-TRACK) was developed by
23 integrating the WRF mesoscale, the STAR-CCM+ street scale and the FLEXPART

1 particle dispersion models, and applied to the Jinshui District of Zhengzhou city, Henan
2 Province. Zhengzhou is located in the central of China with four distinct seasons.
3 According to the Oceanic Niño Index (ONI), an El Niño event occurred in January 2019.
4 The occurrence of El Niño generally favours a warm winter and weak winter winds in
5 China that is conducive to occurrence of air pollution. Therefore, the period of January
6 2019 was selected and simulated for this study. This manuscript is organized as follows.
7 Section 2 presents the model details and the observed data for the model validation. Section
8 3 provides the details of the model validation results, the wind environment characteristics
9 and the ~~potential impact~~[potential contribution](#) of traffic source on receptor sites in the
10 region. Section 4 provides the conclusions of the study.

11 **2. Data and Methods**

12 **2.1 S-TRACK description**

13 The S-TRACK system consists of three major components (Fig. 1). The WRF model
14 is used to obtain the mesoscale three dimensions (3D) meteorological fields, with the initial
15 and boundary conditions provided by NCEP FNL reanalysis data. The STAR-CCM+,
16 driven by the meteorological data from WRF, is used to compute the refined 3D street-
17 level meteorological fields with a resolution of 1 m to 100 m in the simulation area. With
18 the refined 3D meteorology, the FLEXPART model is run to analyse the transports of
19 traffic sources at street-level and their potential contribution to specific sites. One should
20 note that some meteorological variables needed by FLEXPART that the STAR-CCM+
21 cannot provide (Table 1) are obtained from WRF simulations. The specific coupling
22 scheme of the S-TRACK system is detailed as follows:

1 **I. Run the WRF model** (refer to Section 2.2 for specific settings) to obtain
2 meteorological data with a spatial resolution of 1 km × 1 km, including temperature,
3 pressure, humidity, wind, etc.

4 **II. Extract the value of temperature (T) and wind (U, V and W)** from the WRF
5 simulation, as the initial and boundary conditions of the STAR-CCM+ simulation. Run the
6 STAR-CCM+ (refer to Section 2.3 for specific settings) to obtain values of meteorological
7 variables with a spatial resolution of 1 m - 100 m, including wind field, surface pressure,
8 and surface sensible heat flux, etc. The 3D street-level grid for STAR-CCM+ is detailed
9 in Section 2.3.1.

10 **III. Match the STAR-CCM+ grids to the WRF grids.** As the FLEXPART-WRF
11 (version 3.3.2) was used here, the grid structure of meteorological input data to
12 FLEXPART should match the grid structure of WRF model. To this end, a regular fine
13 grid with a horizontal resolution of 10×10 m was constructed based on the pre-processing
14 system of WRF model (WPS). The urban building height data obtained based on drone
15 aerial photography was taken as part of the terrain height data in the WPS. Once the refined
16 grid was established, the meteorological variables of the STAR-CCM+ and WRF model
17 were interpolated into the grid by a nearest-neighbour interpolation method.

18 **IV. Run the backward FLEXPART model** (refer to Section 2.4 for specific settings)
19 to obtain the 3D spatial location data of released particles, which was used to analyse the
20 features of pollutant transport at street-level and potential contribution of traffic source to
21 specific sites.

1 2.2 WRF model configuration

2 In this study, the WRF model is configured with four nested domains (Fig. 2a), with
3 the resolution of 27 km × 27 km (85 × 85 grids [cells](#)), 9 km × 9 km (82 × 82 grids [cells](#)),
4 3 km × 3 km (82 × 82 grids [cells](#)), and 1 km × 1 km (61 × 61 grids [cells](#)), respectively.
5 Vertically, there are 45 full eta levels from the surface to 100 hPa with 11 levels below 2
6 km, on which the meteorological fields are used to drive the STAR-CCM+. The innermost
7 nested region is shown in Fig. 2b, where the area focused in this study is marked with a
8 black box. The initial and boundary conditions of WRF model are obtained from the NCEP
9 re-analysis data (<http://rda.ucar.edu/dataset-s/ds083.2>). The boundary conditions are
10 updated every 6 hr. Table 2 lists the selected physical parameterization schemes. The time
11 from 12:00 Beijing time (BJT) on December 30, 2018 to 23:00 BJT on January 31, 2019
12 is chosen as the modelling period, with the simulation results recorded every hour.

13 2.3 STAR-CCM+ configuration

14 The STAR-CCM+, one of the most commonly used commercial CFD software, was
15 selected for the street-level simulation. Previous studies had found an excellent correlation
16 between STAR-CCM+ simulated and measured values in simulating environmental and
17 meteorological problems at street-level (Santiago et al., 2017;Borge et al., 2018;Jls et al.,
18 2020). The model has functions such as geometric modelling, model pre-processing, the
19 calculation execution, and post-processing of results. More details on STAR-CCM+ can
20 be found at
21 [https://www.plm.automation.siemens.com/global/zh/products/simcenter/STAR-](https://www.plm.automation.siemens.com/global/zh/products/simcenter/STAR-CCM.html)
22 [CCM.html](https://www.plm.automation.siemens.com/global/zh/products/simcenter/STAR-CCM.html).

1 2.3.1 3D street-level grid generation

2 The establishment of a 3D geometric model is based on the actual terrain and
3 buildings height data for the simulated area obtained through the drone aerial photography
4 technology. The basic data such as the geometric shape of urban buildings, roof height and
5 vector data of the top of buildings with high resolution, high timeliness and accuracy are
6 used to construct a realistic 3D geometric model for driving the STAR-CCM+ simulation.
7 In the process of model construction, the same shape as the actual building was maintained
8 to reduce the influence of model errors on the calculation results (Fig. 3a). The length,
9 width, and height of the STAR-CCM+ calculation domain are 13 km, 11 km, and 2 km,
10 respectively, among which, nearly 2/3 of the buildings are distributed in the range of 10 -
11 40 meters, with the average height of the buildings of 32 m. The highest building in the
12 area is 390 m, and the lowest building is 6 m.

13 The geometric model domain is divided by polyhedral meshes (Fig. 3c). The
14 polyhedral mesh has much fewer cells than the traditional tetrahedral mesh, but with a
15 similar accuracy of calculation. Under the same number of grid cells, the numerical
16 simulation results of polyhedral grids [cells](#) are more consistent with experimental data than
17 tetrahedral grid cells (Zhang et al., 2020). The grid cells on the ground and near the
18 buildings are much denser (Fig. 3b) (the minimum resolution is about 1 m), so that the
19 influence of the building on the flow patterns can be described more accurately. In the end,
20 the number of unit grid cells generated is 382181, and the number of nodes is 1990224.

1 2.3.2 Physical model and boundary conditions

2 The STAR-CCM+ solves the RANS with the realizable $k-\varepsilon$ turbulence closure
3 scheme in this study (Li et al., 2019;Li et al., 2006;Lei et al., 2004). The ground and
4 building surfaces are set to be no-slip, and the distribution of fluid velocity and pressure
5 near the ground and the building surface is described by the blended wall function. For the
6 coupling of WRF model to STAR-CCM+, the values of temperature and wind from the
7 WRF simulation are extracted to establish the initial and boundary conditions for STAR-
8 CCM+. Since the variables obtained by WRF simulation have a relatively coarse resolution
9 of 1 km, the velocity components (U, V and W) and the temperature are interpolated to the
10 boundary of STAR-CCM+ domain using the spline interpolation method and the linear
11 interpolation method, respectively. For the turbulence intensity and turbulence viscosity
12 ratio, the lateral and upper boundaries are set as constants with values of 0.1 and 10,
13 respectively.

14 2.4 FLEXPART configuration

15 The simulation area is set to sub-domain B in Figure 3, with a horizontal grid
16 resolution of $10\text{ m} \times 10\text{ m}$. The simulation time is from 1:00 BJT 1 January 2019 to 23:00
17 BJT 30 January 2019. The time step of FLEXPART is 1 s, and the output time interval is
18 120 s. ~~FLEXPART calculates particle trajectories using analysed winds plus random
19 motions in order to account for turbulence. Simulation results from mesoscale
20 meteorological models (such as WRF) do not resolve individual turbulence cells, although
21 they reproduce the large scale effects of turbulence. To account for sub-grid turbulence,
22 turbulence options need to turn on in FLEXPART (Stohl and James, 2004). However in~~

1 ~~this study, the turbulence options are turned off, since the turbulence is already resolved~~
2 ~~by the STAR-CCM+ simulation.~~ Through backward trajectory simulation, the impact of
3 traffic source on the receptor sites in the region can be effectively analysed. Due to the
4 high number of grids cells in the region and the fact that increasing the number of released
5 particles leads to consuming more computational resources, the particle residence time is
6 set as 2 h, and 5 tracer particles are released per hour, and the total number of particles
7 released was 3590 ~~tracer particles in the course of simulation.~~

8 **2.5 Meteorological observation data**

9 Hourly near-surface meteorological observations from the Bank School City
10 monitoring site (hereinafter referred as the BSC monitoring site), including 2 m
11 temperature (T), 2 m relative humidity (RH), surface pressure (P), 10 m wind direction
12 (WD) and 10 m wind speed (WS) in January 2019 are used to evaluate the WRF and
13 STAR-CCM+ simulation results, with the statistical indexes including Pearson's
14 correlation coefficient (R), root mean square error (RMSE), mean bias (MB) and mean
15 error (ME). The location of the BSC monitoring site (34.802375N, 113.675237E) is shown
16 in Figure 3.

17 **3. Results and discussions**

18 **3.1 Model evaluation**

19 The performance of WRF model to simulate meteorological elements is an important
20 basis for STAR-CCM+ and FLEXPART simulations. The hourly meteorological data for
21 January 2019 obtained from the innermost nested simulation of the WRF model is selected

1 to compare with observation data to verify the WRF model. Table 3 lists the statistical
2 results of T, RH, P, and WS. The T and RH are slightly underestimated, with the MB
3 values as -1.86 k and -5.95% , respectively, and the P and WS are overestimated by the
4 WRF model, with the MB values as 3.66 hPa and 1.44 m s^{-1} , respectively. The R values
5 for T, RH and P are 0.80 , 0.70 and 0.98 , respectively, passing the 99% significance test
6 ([see Appendix 2](#)), and indicating that the variation characteristics of T, RH and P are well
7 reproduced by the WRF model. WS is generally overestimated by WRF model (Temimi
8 et al., 2020;He et al., 2014), which is also found in the present study with the RMSE of
9 1.97 m s^{-1} . The performance of the near-surface meteorology obtained by the WRF
10 simulation is equivalent to previous studies (He et al., 2017b;Carvalho et al., 2012).

11 Since the time-varying boundary conditions in the calculation domain of STAR-
12 CCM+ are obtained from WRF model, the simulation performance of WRF model has an
13 important influence on the STAR-CCM+ simulation results. The wind has an important
14 influence on the transport of air pollutants in the area (Zhang et al., 2015). Figure 4 shows
15 the hourly wind observations and simulations at the BSC monitoring site in January 2019.
16 Both WRF and STAR-CCM+ overestimate the wind speed to certain degrees (Fig. 4a).
17 The average of observed wind speed is 0.92 m s^{-1} , ~~with and~~ the [average of value](#) simulated
18 [value](#) by WRF and ~~by~~ STAR-CCM+ is 2.37 m s^{-1} and 2.00 m s^{-1} , respectively. The R
19 values of WRF and STAR-CCM+ are 0.45 and 0.67 , respectively, passing the 99%
20 significance test, and demonstrating the refined STAR-CCM+ wind simulations are
21 superior to that of the WRF. This might be due to the fact that the resolution of WRF
22 simulation is not fine enough and the underlying surface is processed in a parameterized
23 way that can't accurately describe the urban surface roughness. For the STAR-CCM+, the

1 geometric model is used for the underlying surface, which could better reflect the urban
2 surface conditions compared to parametric methods. Figure 4b shows the comparison
3 results of the observed and simulated wind directions. It can be seen that the change of the
4 wind direction is captured by the STAR-CCM+ well. The wind direction is verified by hit
5 rates (HR) (Schlünzen and Sokhi, 2008), [which is a reliable overall measure for describing](#)
6 [model performance \(see Appendix 4\)](#). With desired accuracy between $\pm 45^\circ$, the HR are
7 calculated at 63 and 51 % for STAR-CCM+ and WRF, respectively, indicating that
8 variations in wind direction have been basically captured with a better performance for
9 STAR-CCM+ simulations.

10 **3.2 The characteristics of the street-level wind fields**

11 In urban areas, the complex spatial structure and layout of buildings have a great
12 influence on the street-level wind field (Liu et al., 2018; Park et al., 2015), which is a crucial
13 meteorological factor that controls the transport of air pollutants. The street-level wind
14 field characteristics were simulated by the S-TRACK and discussed comprehensively in
15 this paper for the overall average in January as well as for different background wind
16 directions, i.e., north, south, west and east, respectively.

17 **3.2.1 The average wind field characteristics**

18 Figures 5a-b illustrate the distribution of the average wind streamlines in January at
19 the height of 5 m and 40 m, respectively. At the height of 5 m, the wind field structure is
20 more complicated (Fig. 5a) than that at 40 m (Fig. 5b). The wind speed is relatively more
21 intense in the areas where the buildings are sparse and smaller. In addition, the flow fields
22 diverge or converge due to the layout of buildings and streets, causing the wind direction

1 inside blocks differ from the background wind direction greatly. As the density of
2 buildings gradually decreases with the increases of height, this phenomenon diminishes,
3 reflected by the relatively more consistent wind fields at 40 m (Fig. 5b). The phenomenon
4 was also found in a previous study (Sui et al., 2016).

5 To clearly show the details of the wind field, a sub-domain A (Fig. 3a) with complex
6 building structures is selected from the entire computational domain. The near-surface
7 winds disperse or converge horizontally and rise or subsidence vertically with the building
8 (Fig. 5c). During the climb or fall with the building, downwash winds with high wind
9 speeds occur (as shown in the red dashed circles). Due to the complexity of the building
10 layout, local circulation is formed on the west side of the BSC monitoring site, making the
11 airflow around the building on the south side of the station accumulate and forms an
12 obvious convergence area (Fig. 5c), which is not conducive to the air circulation and
13 pollution transport (as shown in the red box).

14 **3.2.2 The wind field characteristics under different background wind directions**

15 Figure 6 shows the distributions of near-surface wind and its divergence under four
16 different background wind directions. In general, the overall wind direction in the area is
17 consistent with the background wind direction, but the airflow near-surface is significantly
18 affected by the building layout, thus forming local circulations with divergence or
19 convergence zones. The wind speeds in the areas with dense buildings are significantly
20 smaller than those in open areas (Figs. 6a-1, 6b-1, 6c-1, and 6d-1), which is attributed to
21 the obvious frictional dragging effect of the dense buildings. The overall wind direction in
22 the area is generally the same as the background wind direction, but the airflow is diverged

1 or converged by the influence of the building layout, resulting in a great difference in wind
2 direction inside the block from the background. When the background wind direction is
3 north or west (Figs. 6b and 6c), the overall wind speed in the area is relatively large. This
4 is mainly due to the temperate monsoon climate in Zhengzhou, where northwest and west
5 winds prevail in winter and wind speeds are relatively high.

6 It is found that the windward side of the building is mostly a divergence zone and the
7 leeward side is mainly a convergence zone, which is more obvious for higher buildings.
8 When the airflow meets the building, the airflow on the windward side of the building is
9 blocked and thus spreads outward, forming a divergence zone; while the airflow on the
10 leeward side of the building converges and generates a vortex with lower wind speed,
11 forming a convergence zone. For example, at BSC monitoring site, when the background
12 wind direction is west, the wind speed on the windward side of the building is higher and
13 diffused outward by the building blockage (Fig. 6c-2), resulting in a significant divergence
14 zone (Fig. 6c-3). High-rise buildings have a greater impact on the wind field and cause a
15 strong degree of convergence and divergence. It can be seen that the degree of divergence
16 or convergence around the high-rise building is more significant than those around low
17 buildings in the area (Figs. 6b-3, 6c-3, and 6d-3). In addition, the ventilation is better when
18 the dominant airflow is in the same direction as building layout (Fig. 6c). In the process of
19 urban construction, the influence of prevailing wind direction on the layout of buildings
20 should be considered, which could effectively improve the efficiency of urban ventilation.

3.3 ~~Potential impact~~ Potential contribution of traffic sources

In this section, the S-TRACK system is used to analyse ~~potential impact~~ potential contribution of main traffic roads (R1-R4) in sub-domain B (Fig. 3a) on several receptor sites nearby with different heights and locations with a number of schools and residential areas. The widths of roads R1-R4 are about 45, 33, 20 and 18 meters, respectively. ~~During January 2019, the average traffic volumes were about 2300 (R1), 490 (R2), 400 (R3) and 90 (R4) cars per hour, respectively.~~ Since the detailed information on road traffic emissions was not available, the road traffic emissions were assumed to be uniformly distributed and with identical intensity in this study. During the backward trajectory simulation, the particles as long as passing within 5 m height above the road is considered to be a potential contribution from the road emissions to the receptor site. Additionally, ~~the potential impact~~ potential contribution of traffic source under different background wind directions was also explored. The residence-time analysis (RTA), which has been previously used to identify the accounted contribution of emission sources to air quality of receptors (Yu, 2017; Salvador et al., 2008; Hopke et al., 2005; Poirot et al., 2001; Ashbaugh et al., 1985), was selected in this study to assess the potential contribution ratio (PCR) of the traffic source on receptors. The RTA is expressed as:

$$R_{i,j} = \frac{\tau_{i,j}}{t},$$

where $R_{i,j}$ indicates the contribution ratio of the grid (i,j) to receptor; $\tau_{i,j}$ means the residence time in the grid (i,j) and t means the total residence time in all grids cells.

3.3.1 ~~Potential impact~~Potential contribution of traffic source at different sites in winter

In order to analyse the ~~potential impact~~potential contribution of the traffic source on different locations, the receptor sites were selected at different locations and heights, and the overall ~~potential contribution ratio~~PCR of all wind directions for January 2019 was calculated by RTA (Table 4). Receptor sites S2-S8, with identical horizontal location but different heights, are selected to investigate contributions of traffic source to receptor sites at different heights. The ~~potential contribution ratios~~PCR of all the four roads are 4.05%, 4.25%, 4.33%, and 4.67% for receptor sites S2 to S5, with the height of 2 m, 5 m, 10 m, and 15 m, respectively. However, as the receptor height continues to rise, namely from S5 to S8, the ~~potential contribution ratios~~PCR of the roads gradually decrease from 4.67% to 3.55% (Table 4). It's noteworthy that the contributions from R1 and R3 are primary, especially the R1, which may be due to the closer distance to the site and the generally northeast wind field. The ~~potential impact~~potential contribution of the traffic source is the greatest when the receptor site is located at a height of 15 m, suggesting the air quality at that height is most susceptible to traffic emissions under the northeast wind field. In addition, according to density distribution (refers to the number of particles that have stayed in the space of 10 m × 10 m in the horizontal direction and 5 m from the surface to above in the vertical direction) of all trajectory points that have passed through the traffic roads (Figs. 7), it can be seen that the road section with large ~~potential impact~~potential contribution to the receptor sites generally located to their northeast, which might be a result of the combination effect of the background wind field and the building layout. For more details, the vertical structure of winds along the direction of the wind field at the

1 receptor site S2 (Fig. 8b) is also presented. It can be seen that there is a general upward
2 motion in the airflow, making the position with the greatest ~~potential contribution~~
3 ~~ratio~~PCR from traffic source locate at a certain height, which is about 15 m over the
4 receptor site S2 in this case.

5 It can be seen from Table 4 that R1 is the road with the greatest ~~potential~~
6 ~~impact~~potential contribution to the receptor sites. The horizontal distance between road R1
7 and the receptor sites is about 300 m and the peak of the ~~potential contribution ratios~~PCR
8 occurs at a height of about 15 m (corresponding to the site S5). However, for the road R3,
9 which is closest to the receptor sites in horizontal (about 200 m), the contribution ratios
10 are lower than those of the road R1. Figure 8a shows that the near ground winds are
11 generally northeast, resulting in that the probability of traffic contributions from R1 and
12 R3 road sections upwind of the site S2 is roughly the same. Nonetheless, as mentioned in
13 section 3.3, the width for the road R1 is about twice of that for the road R3. Therefore,
14 even R1 was a little farther from the receptor sites than R3, the contribution ratios of R1
15 to the sites were calculated larger than those of R3. For the R2 and R4, the distance from
16 the receptor sites is about 1200 and 1500 m, respectively, far away than those of R1 and
17 R3. In addition, under the northeast winds, traffic source was hardly transported to the
18 receptor sites, rendering the contribution ratios quite small below 50 m (Table 4). It can
19 also be seen, from Table 4, that the corresponding ~~potential contribution ratios~~PCR of R2
20 and R4 may peak at a height over 50 m.

21 Since the road R1 had the largest potential contribution to the receptor sites, the
22 contribution of R1 to different positions is focused in the subsequent discussion. For the
23 receptor site S1, which is about 400 m from the R1, located in a dense building area with

1 the building height at 30 to 40 meters, the ~~potential contribution ratio~~PCR of the traffic
2 source on the receptor site is calculated to be 1.81%. For the receptor site S2, which is
3 about 300 m from the traffic road, located in an open area and surrounded by low buildings,
4 the ~~potential contribution ratio~~PCR of the traffic source is determined to be 2.38%. It might
5 be inferred that the wind field difference partially resulted from the influence of buildings
6 layout led to the higher contribution ratio to S2. From the average wind field in January
7 2019 (Fig.8a), it can be seen that the winds were influenced by high-rise buildings around
8 the S1, resulting in a change in transport path of pollutants and thus, making pollutants
9 difficult to reach the S1 site. However, for S2 site, the winds were less influenced by the
10 buildings and pollutants were more easily transported there.

11 ~~Potential impact~~Potential contribution of traffic source under different 12 background wind directions

13 In order to investigate the ~~potential impact~~potential contribution of traffic source
14 under different background wind directions, the receptor site S2 influenced by the R1
15 under the east, the south, the west, and the north wind directions was classified from the
16 simulation period. The ~~potential contribution ratios~~PCR of traffic source were estimated
17 to be 2.45%, 0.07%, 1.98%, and 2.97% for the east, the south, the west, and the north wind
18 directions, respectively, revealing that the difference in ~~potential impact~~potential
19 contribution was largest between the south and north wind directions. When the
20 background wind direction was south, the receptor site was located upwind of the road,
21 and the road traffic source contributed very little to the receptor site. On the contrary, when
22 the receptor site was downwind of the road with northern winds, the contribution ratio of

1 road traffic source to the receptor site was the greatest. When the background wind
2 direction was east and west, the contribution ratio to the receptor point was similar, ranging
3 between the ratios under south and north wind directions. The lower contribution ratio
4 during westerly winds relatively to that under easterly winds might partially be due to the
5 denser distribution of buildings upwind of the receptor site. Complex building layouts
6 changed the structure of the wind field and thus had an impact on the transport of pollutants.
7 The slow air circulation in dense building areas made it unfavourable for pollutants to be
8 transported. In the windward side of the dense building area, the wind was blocked and
9 diverted to both sides of the building. Pollutants were difficult to transport to the leeward
10 side of the building, where the receptor site was located. The results of the [potential](#)
11 [impact potential contribution](#) of traffic source under different background wind conditions
12 is helpful to understand the street-level pollution transport characteristics and provides
13 effective suggestions for the traffic pollution control strategies.

14 **4. Conclusions**

15 A street-level pollutant tracking system has been developed to simulate micro-scale
16 meteorology and used to analyse the characteristics of wind environment and the potential
17 traffic source contribution of air pollution to receptors through backward simulations in a
18 city district. In general, the S-TRACK system is effective in simulating the street-level
19 meteorological and pollution problems. The presence of buildings has a significant effect
20 on the wind environment, i.e., the dragging effect of dense buildings renders the wind
21 speed inside the block smaller than the background wind speed. The ventilation is better
22 when the dominant airflow is consistent with the direction of building layout. Influenced

1 by the building layout, the airflow near-surface is formed with divergence and convergence
2 zones. The windward side of the building is mostly a divergence zone and the leeward side
3 is mostly a convergence zone, which is more obvious for higher buildings.

4 As a test case, the S-TRACK system has been used to investigate the ~~potential~~
5 ~~impact~~potential contribution of traffic source on receptor sites with different locations,
6 heights and background wind directions in a city district. ~~The potential impact of traffic~~
7 ~~sources on a specific receptor site varies under different background wind directions,~~
8 ~~which are estimated to be 2.45%, 0.07%, 1.98%, and 2.97% for the east, the south, the~~
9 ~~west, and the north wind directions, respectively. The difference in potential contribution~~
10 ~~under east and west wind directions might partially be due to the density of buildings~~
11 ~~upwind of the receptor site.~~ For a specific location of this case study, the potential traffic
12 contribution ratios also varied with height at about 4.05%, 4.25%, 4.33%, 4.67%, 4.38%,
13 3.64% and 3.55% for 2, 5, 10, 15, 20, 40, 50 m, respectively, manifesting a significant
14 trend of increasing and then decreasing with height. In addition, the height of position with
15 the greatest ~~potential contribution ratio~~PCR from the traffic source varies jointly
16 influenced by the distance between the position and traffic source, as well as the
17 background wind field. ~~The potential contribution of traffic sources on a specific receptor~~
18 ~~site varies under different background wind directions, which are estimated to be 2.45%,~~
19 ~~0.07%, 1.98%, and 2.97% for the east, the south, the west, and the north wind directions,~~
20 ~~respectively. The difference in potential contribution under east and west wind directions~~
21 ~~might partially be due to the density of buildings upwind of the receptor site.~~

22 In the future, in-depth simulation experiments with different building layouts, wind
23 field environments, and distances between traffic source and receptor are required to

1 quantify the ~~potential impact~~potential contribution of street-level pollution sources and to
2 establish the relationship between meteorological conditions, buildings and various
3 emissions (point, area and line sources) in the street-level for an effective management of
4 regional pollution in a city.

5 **Appendix**

6 **1. Some settings to improve the calculations efficiency of CFD**

7 It is true that using a CFD model for the atmospheric numerical simulation has the
8 problem of high computational cost. In this study, the RANS is chosen as the CFD
9 preprocessing model, which requires relatively small amount of computational resources.
10 The time step of STAR-CCM+ is set to 60s, with a maximum of 20 internal iterations in
11 each time step and a parallel computing with 32 CPUs is done on a supercomputer. The
12 simulation error increases with the simulation time. In order to ensure the efficiency and
13 accuracy of the simulation, the month was divided into four time periods to simulate, as
14 shown in Table A1.

15 **Table A1. The division of each simulation time period and the physical time spent on the simulation**

Simulation start time	Simulation end time	Length of simulation time	Physical time spent
2018/12/31 00:00:00	2019/1/09 04:00:00	220h	126.45h
2019/1/08 00:00:00	2019/1/17 04:00:00	220h	128.33h
2019/1/16 00:00:00	2019/1/25 04:00:00	220h	128.53h
2019/1/24 00:00:00	2019/2/01 08:00:00	200h	117.10h

16

2. Significance test

Significance test is used to determine the significance of the results in relation to the null hypothesis, with a p-value, or probability value describing how likely the data would have occurred by random chance (i.e. that the null hypothesis is true). A p-value less than 0.05 (typically ≤ 0.05) is statistically significant. It indicates strong evidence against the null hypothesis, as there is less than a 5% probability the null is correct.

3. The observed data for January 2019 at various meteorological stations in Zhengzhou city.

Table A2. The location of each meteorological station and the average wind speed.

number	Latitude and longitude coordinates	Average wind speed
1	(34.7274 N, 113.7493 E)	0.92 m s ⁻¹
2	(34.73506 N, 113.6457 E)	0.92 m s ⁻¹
3	(34.7466 N, 113.6876 E)	1.32 m s ⁻¹
4	(34.76117 N, 113.6883 E)	0.61 m s ⁻¹
5	(34.78245 N, 113.6567 E)	1.51 m s ⁻¹
6	(34.81151 N, 113.6948 E)	1.48 m s ⁻¹
7	(34.83267 N, 113.5453 E)	0.72 m s ⁻¹

4. Hit rates

The hit rate is a reliable overall measure for describing model performance.

$$H = \frac{100}{m} \times \sum_{i=1}^m n_i$$

$$\text{with } n_i = \begin{cases} 1 & \text{for } |\text{difference (measurement,} \\ & \text{model result)}| < A \\ 0 & \text{for } |\text{difference (measurement,} \\ & \text{model result)}| > A \end{cases}$$

where m is the number of comparison data, A is to consider the desired model accuracy.

The single hit rate is calculated ranging from 100% if all model results are within A of the observations to 0% if none are.

Formatted: Font: 四号

Field Code Changed

Formatted: Font: 四号

54. Divergence

The divergence is a quantity that describes the degree to which air converges from its surroundings to a point or flows away from a point. It is used to describe the intensity of divergence and convergence at locations in space. The formula is as follows.

$$\text{div } \mathbf{v} = \nabla \cdot \mathbf{v} = \frac{\partial u}{\partial x} + \frac{\partial v}{\partial y} + \frac{\partial w}{\partial z},$$

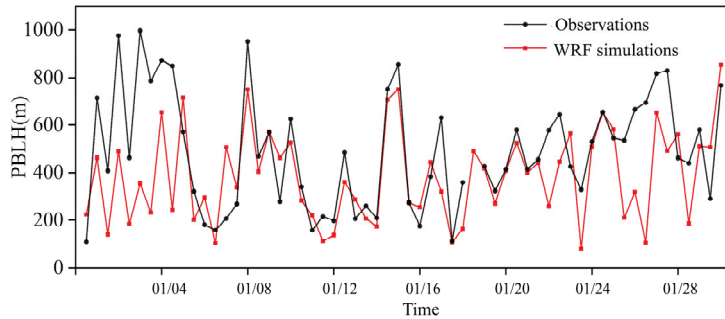
where u , v and w are the components of the wind in the x , y and z direction, respectively. When the $\text{div } \mathbf{v} < 0$, the location is convergence; when the $\text{div } \mathbf{v} > 0$, the location is divergence.

65. PBLH validation

The bulk Richardson number (Ri) method was taken to estimate the BLH base on the sounding data of Zhengzhou. Ri is expressed as:

$$R_i(z) = \frac{(g / \theta_s)(\theta_z - \theta_s)(z - z_s)}{(u_z - u_s)^2 + (v_z - v_s)^2 + (bu_s^2)},$$

where z is the height above ground, s the surface, g means the acceleration of gravity, θ the virtual potential temperature, u and v the component of wind speed, and u_s the surface friction velocity. u_s can be ignored here due to it is small relative to the wind shear (Vogelezang and Holtslag, 1996). Previous theoretical and laboratory studies suggested that when Ri is smaller than a critical value (~ 0.25), the laminar flow becomes unstable (Stull, 1988). Therefore, the lowest level z at which the interpolated Ri exceeds the critical value of 0.25 is referred to as PBLH in this study, which is referred to the criterion used by Seidel et al. (2012). The R value is 0.57, passed the 99% significance test. It can be seen from Figure A1 that the variation of boundary layer height is generally captured.



1

2 **Figure A1. Time series of the observed (black) and simulated (red) PBLH at 8:00 and 20:00 Beijing**
 3 **time (BJT) in Zhengzhou sounding site.**

4

5 **Code/data availability**

6 All source code and data can be accessed by contacting the corresponding authors Sunling
 7 Gong (gongsl@cma.gov.cn) and Lei Zhang (leiz09@cma.gov.cn).

8 **Authors contribution**

9 Sunling Gong and Lei Zhang designed the research. Huan Zhang performed the
 10 simulations and wrote the manuscript with suggestions from all authors. Jingyue Mo,
 11 Huabing Ke, Xu Wang, and Shuhua Lu assisted with data processing. Jianjun He,
 12 Yaqiang Wang, Jingwei Ni and Lixin Shi participated in the scientific interpretation and
 13 discussion. All authors contributed to the discussion and improvement of the manuscript.

14 **Competing interests**

15 The authors declare that they have no conflict of interest.

1 **Acknowledgments**

2 The authors would like to acknowledge Bin Cui and Lin Zhang from Peking University
3 and Liangfu Chen from Chinese Academy of Sciences for their valuable suggestions to
4 improve the article.

5

1 References

- 2 Ashbaugh, L., Malm, W., and Sadeh, W.: A residence time probability analysis of sulfur concentrations at grand Canyon
3 national park, *Atmos. Environ.*, 19, 1263-1270, [https://doi.org/10.1016/0004-6981\(85\)90256-2](https://doi.org/10.1016/0004-6981(85)90256-2), 1985.
- 4 Aynsley, R.: Politics of pedestrian level urban wind control, *Build Environ*, 24, 291-295, <https://doi.org/10.1016/0360->
5 [1323\(89\)90022-X](https://doi.org/10.1016/0360-1323(89)90022-X), 1989.
- 6 Borge, R., Jose Luis Santiago, David de la Paz, Fernando Martín, Jessica Domingo, Cristina Valdés, Beatriz Sánchez, Esther
7 Rivas, Ma Teresa Rozas, Sonia Olaechea Lázaro, Pérez, J., and Fernández., a. Á. L.-P.: Application of a short term air quality
8 action plan in Madrid (Spain) under a high-pollution episode - Part II: Assessment from multi-scale modelling, *Sci. Total*
9 *Environ.*, 635, 1574-1584, <https://doi.org/10.1016/j.scitotenv.2018.04.323>, 2018.
- 10 Brioude, J., Arnold, D., Stohl, A., Cassiani, M., Morton, D., Seibert, P., Angevine, W., Evan, S., Dingwell, A., Fast, J. D.,
11 Easter, R. C., Pisso, I., Burkhardt, J., and Wotawa, G.: The Lagrangian particle dispersion model FLEXPART-WRF version
12 3.1, *Geosci. Model Dev. (GMD)*, 6, 1889-1904, <https://doi.org/10.5194/gmd-6-1889-2013>, 2013.
- 13 Carvalho, D., Rocha, A., Gómez-Gesteira, M., and Santos, C.: A sensitivity study of the WRF model in wind simulation for
14 an area of high wind energy, *Environ. Model. Software*, 33, 23-34, <https://doi.org/10.1016/j.envsoft.2012.01.019>, 2012.
- 15 Cécé, R., Bernard, D., Brioude, J., and Zahibo, N.: Microscale anthropogenic pollution modelling in a small tropical island
16 during weak trade winds: Lagrangian particle dispersion simulations using real nested LES meteorological fields, *Atmos.*
17 *Environ.*, 139, 98-112, <https://doi.org/10.1016/j.atmosenv.2016.05.028>, 2016.
- 18 Chen, F., and Dudhia, J.: Coupling an Advanced Land Surface-Hydrology Model with the Penn State-NCAR MM5 Modeling
19 System. Part I: Model Implementation and Sensitivity, *Mon. Weather Rev.*, 129, 569-585, <https://doi.org/10.1175/1520->
20 [0493\(2001\)129<0569:CAALSH>2.0.CO;2](https://doi.org/10.1175/1520-0493(2001)129<0569:CAALSH>2.0.CO;2), 2001.
- 21 de Foy, B., Burton, S. P., Ferrare, R. A., Hostetler, C. A., Hair, J. W., Wiedinmyer, C., and Molina, L. T.: Aerosol plume
22 transport and transformation in high spectral resolution lidar measurements and WRF-Flexpart simulations during the
23 MILAGRO Field Campaign, *Atmos. Chem. Phys.*, 11, 3543-3563, <https://doi.org/10.5194/acp-11-3543-2011>, 2011.
- 24 Ehrhard, J., Khatib, I., Winkler, C., Kunz, R., Moussiopoulos, N., and Ernst, G.: The microscale model MIMO: development
25 and assessment, *J. Wind. Eng. Ind. Aerodyn.*, 85, 163-176, [https://doi.org/10.1016/S0167-6105\(99\)00137-3](https://doi.org/10.1016/S0167-6105(99)00137-3), 2000.
- 26 Fast, J. D., and Easter, R. C.: A Lagrangian particle dispersion model compatible with WRF, 7th WRF Users Workshop,
27 NCAR, 19-22, 2006.
- 28 Fernando, H., Zajic, D., Sabatino, S. D., Dimitrova, R., and Dallman, A.: Flow, turbulence, and pollutant dispersion in urban
29 atmosphere, *Phys. Fluids*, 22, 051301, <https://doi.org/10.1063/1.3407662>, 2010.
- 30 Gao, Y., Shan, H., Zhang, S., Sheng, L., Li, J., Zhang, J., Ma, M., Meng, H., Luo, K., Gao, H., and Yao, X.: Characteristics
31 and sources of PM_{2.5} with focus on two severe pollution events in a coastal city of Qingdao, China, *Chemosphere*, 247,
32 125861, <https://doi.org/10.1016/j.chemosphere.2020.125861>, 2020.
- 33 Gosman, A. D.: Developments in CFD for industrial and environmental applications in wind engineering, *J. Wind. Eng. Ind.*
34 *Aerodyn.*, 81, 21-39, [https://doi.org/10.1016/S0167-6105\(99\)00007-0](https://doi.org/10.1016/S0167-6105(99)00007-0), 1999.
- 35 He, J., Mao, H., Gong, S., Yu, Y., and Zou, C.: Investigation of particulate matter regional transport in Beijing based on
36 numerical simulation, *Aerosol Air Qual. Res.*, 17, 1181-1189, <https://doi.org/10.4209/AAQR.2016.03.0110>, 2017a.
- 37 He, J., Zhang, L., Yao, Z., Che, H., Gong, S., Wang, M., Zhao, M., and Jing, B.: Source apportionment of particulate matter
38 based on numerical simulation during a severe pollution period in Tangshan, North China, *Environ. Pollut.*, 266, 115133,
39 <https://doi.org/10.1016/j.envpol.2020.115133>, 2020.
- 40 He, J. J., Yu, Y., Liu, N., Zhao, S. P., and Chen, J. B.: Impact of land surface information on WRFs performance in complex
41 terrain area, *Chin. J. Atmos. Sci.*, 38, 484-498, <https://doi.org/10.3878/j.issn.1006-9895.2013.2014>, 2014.
- 42 He, J. J., Yu, Y., Yu, L. J., Liu, N., and Zhao, S. P.: Impacts of uncertainty in land surface information on simulated surface
43 temperature and precipitation over China, *Int J Climatol*, 37, 829-847, <https://doi.org/10.1002/joc.5041>, 2017b.
- 44 Hendricks, E. A., Diehl, S. R., Burrows, D. A., and Keith, R.: Evaluation of a Fast-Running Urban Dispersion Modeling
45 System Using Joint Urban 2003 Field Data, *J Appl Meteorol Climatol*, 46, 2165-2179,
46 <https://doi.org/10.1175/2006JAMC1289.1>, 2007.
- 47 Heo, J., Foy, B. D., Olson, M. R., Pakbin, P., Sioutas, C., and Schauer, J.: Impact of regional transport on the anthropogenic
48 and biogenic secondary organic aerosols in the Los Angeles Basin, *Atmos. Environ.*, 103, 171-179,
49 <https://doi.org/10.1016/j.jatmosenv.2014.12.041>, 2015.
- 50 Hopke, P., Zhou, L., and Poirot, R.: Reconciling trajectory ensemble receptor model results with emissions, *Environ. Sci.*
51 *Technol.*, 39(20), 7980-7983, <https://doi.org/10.1021/es049816g>, 2005.
- 52 Iacono, M. J., Delamere, J. S., Mlawer, E. J., Shephard, M. W., and Collins, W. D.: Radiative Forcing by Long-Lived
53 Greenhouse Gases: Calculations with the AER Radiative Transfer Models, *J. Geophys. Res.-Atmos.*, 113, D13103,
54 <https://doi.org/10.1029/2008JD009944>, 2008.
- 55 Jls, A., Bse, A., Cq, B., Ddlp, B., Am, A., Fm, A., Rb, B., Er, A., Gm, A., and Ed, A.: Performance evaluation of a multiscale
56 modelling system applied to particulate matter dispersion in a real traffic hot spot in Madrid (Spain) - ScienceDirect,
57 *Atmospheric Pollut.*, 11, 141-155, <https://doi.org/10.1016/j.apr.2019.10.001>, 2020.
- 58 Kurppa, M., Hellsten, A., Auvinen, M., Raasch, S., Vesala, T., and Järvi, L.: Ventilation and Air Quality in City Blocks Using
59 Large-Eddy SimulatioZ Urban Planning Perspective, *Atmosphere*, 9, 65, <https://doi.org/10.3390/ATMOS9020065>, 2018.
- 60 Kwak, K.-H., Baik, J.-J., Ryu, Y.-H., and Lee, S.-H.: Urban air quality simulation in a high-rise building area using a CFD
61 model coupled with mesoscale meteorological and chemistry-transport models, *Atmos. Environ.*, 100, 167-177,
62 <https://doi.org/10.1016/j.atmosenv.2014.10.059>, 2015.

1 Lei, L., Fei, H., Cheng, X. L., and Han, H. Y.: The application of computational fluid dynamics to pedestrian level wind safety
2 problem induced by high-rise buildings, *Chin. Phys. B*, 13, 1070-1075, <https://doi.org/10.1088/1009-1963/13/7/018>, 2004.

3 Lei, L. I., Yang, L., Zhang, L. J., and Jiang, Y.: Numerical Study on the Impact of Ground Heating and Ambient Wind Speed
4 on Flow Fields in Street Canyons, *Adv Atmos Sci*, 29, 1227-1237, <https://doi.org/10.1007/s00376-012-1066-3>, 2012.

5 Li, L., Hu, F., Cheng, X. L., Jiang, J. H., and Ma, X. G.: Numerical simulation of the flow within and over an intersection
6 model with Reynolds-averaged Navier-Stokes method, *Chin. Phys. B*, 15, 149-155, <https://doi.org/10.1088/1009-1963/15/1/024>, 2006.

7 Li, S., Sun, X., Zhang, S., Zhao, S., and Zhang, R.: A Study on Microscale Wind Simulations with a Coupled WRF-CFD
8 Model in the Chongli Mountain Region of Hebei Province, China, *Atmosphere*, 10, 731,
9 <https://doi.org/10.3390/atmos10120731>, 2019.

10 Li, X.-X., Liu, C.-H., and Leung, D. Y. C.: Large-Eddy Simulation of Flow and Pollutant Dispersion in High-Aspect-Ratio
11 Urban Street Canyons with Wall Model, *Bound. Layer Meteorol.*, 129, 249-268, <https://doi.org/10.1007/s10546-008-9313-y>,
12 2008.

13 Lin, Y. L., Farley, R. D., and Orville, H. D.: Bulk Parameterization of the Snow Field in a Cloud Model, *J APPL METEOROL*,
14 22, 1065-1092, [https://doi.org/10.1175/1520-0450\(1983\)022<1065:BPOTSF>2.0.CO;2](https://doi.org/10.1175/1520-0450(1983)022<1065:BPOTSF>2.0.CO;2), 1983.

15 Liu, N., Yu, Y., He, J., and Zhao, S.: Integrated modeling of urban-scale pollutant transport: application in a semi-arid urban
16 valley, Northwestern China (SCI), *Atmospheric Pollut. Res.*, 4, 306-314, <https://doi.org/10.5094/APR.2013.034>, 2013.

17 Liu, S., Pan, W., Zhao, X., Zhang, H., Cheng, X., Long, Z., and Chen, Q.: Influence of surrounding buildings on wind flow
18 around a building predicted by CFD simulations, *Build Environ*, 140, 1-10, <https://doi.org/10.1016/j.buildenv.2018.05.011>,
19 2018.

20 Macdonald, R. W., Griffiths, R. F., and Cheah, S. C.: Field experiments of dispersion through regular arrays of cubic structures,
21 *Atmos. Environ.*, 31, 783-795, [https://doi.org/10.1016/S1352-2310\(96\)00263-4](https://doi.org/10.1016/S1352-2310(96)00263-4), 1997.

22 Madala, S., Satyanarayana, A. N., Srinivas, C., and Kumar, M.: Mesoscale atmospheric flow-field simulations for air quality
23 modeling over complex terrain region of Ranchi in eastern India using WRF, *Atmos. Environ.*, 107, 315-328,
24 <https://doi.org/10.1016/J.ATMOSENV.2015.02.059>, 2015.

25 Mavroidis, I., Rf, G., and Dj, H.: Field and wind tunnel investigations of plume dispersion around single surface obstacles,
26 *Atmos. Environ.*, 37, 2903-2918, [https://doi.org/10.1016/S1352-2310\(03\)00300-5](https://doi.org/10.1016/S1352-2310(03)00300-5), 2003.

27 Milliez, M., and Carissimo, B.: Computational Fluid Dynamical Modelling of Concentration Fluctuations in an Idealized
28 Urban Area, *Bound. Layer Meteorol.*, 127, 241-259, <https://doi.org/10.1007/s10546-008-9266-1>, 2008.

29 Nakanishi, M., and Niino, H.: An Improved Mellor-Yamada Level-3 Model: Its Numerical Stability and Application to a
30 Regional Prediction of Advection Fog, *Bound. Layer Meteorol.*, 119, 397-407, <https://doi.org/10.1007/S10546-005-9030-8>,
31 2006.

32 Nelson, M. A., Brown, M. J., Halverson, S. A., Bieringer, P. E., Annunzio, A., Bieberbach, G., and Meech, S.: A Case Study
33 of the Weather Research and Forecasting Model Applied to the Joint Urban 2003 Tracer Field Experiment. Part 2: Gas Tracer
34 Dispersion, *Bound. Layer Meteorol.*, 161, 461-490, <https://doi.org/10.1007/s10546-016-0188-z>, 2016.

35 Park, S. B., Baik, J. J., and Han, B. S.: Large-eddy simulation of turbulent flow in a densely built-up urban area, *Environ. Fluid
36 Mech.*, 15, 235-250, <https://doi.org/10.1007/s10652-013-9306-3>, 2015.

37 Poirot, R., Wishinski, P., Hopke, P., and Polissar, A.: Comparative application of multiple receptor methods to identify aerosol
38 sources in northern Vermont, *Environ. Sci. Technol.*, 35(23), 4622-4636, <https://doi.org/10.1021/es011442t>, 2001.

39 Sada, K., and Sato, A.: Numerical calculation of flow and stack-gas concentration fluctuation around a cubical building, *Atmos.
40 Environ.*, 36, 5527-5534, [https://doi.org/10.1016/S1352-2310\(02\)00668-4](https://doi.org/10.1016/S1352-2310(02)00668-4), 2002.

41 Salvador, P., Artiñano, B., Querol, X., and Alastuey, A.: A combined analysis of backward trajectories and aerosol chemistry
42 to characterise long-range transport episodes of particulate matter: the madrid air basin, a case study, *Sci. Total Environ.*,
43 390(2-3), 495-506, <https://doi.org/10.1016/j.scitotenv.2007.10.052>, 2008.

44 Sandeepan, B., Rakesh, P. T., and Venkatesan, R.: Numerical simulation of observed submesoscale plume meandering under
45 nocturnal drainage flow, *Atmos. Environ.*, 69, 29-36, <https://doi.org/10.1016/J.ATMOSENV.2012.12.007>, 2013.

46 Santiago, J. L., Rafael Borge, Fernando Martín, David de la Paz, Alberto Martilli, Lumbreras, J., and Sánchez, a. B.: Evaluation
47 of a CFD-based approach to estimate pollutant distribution within a real urban canopy by means of passive samplers., *Sci.
48 Total Environ.*, 576, 46-58, <https://doi.org/10.1016/j.scitotenv.2016.09.234>, 2017.

49 Schlünzen, K. H., and Sokhi, R. S.: Overview of Tools and Methods for Meteorological and Air Pollution Mesoscale Model
50 Evaluation and User Training, Joint report by WMO and COST 728, WMO/TD-No. 1457, Geneva, Switzerland, 2008, 2008.

51 Seidel, D. J., Zhang, Y., Beljaars, A., Golaz, J. C., Jacobson, A. R., and Medeiros, B.: Climatology of the planetary boundary
52 layer over the continental United States and Europe, *Journal of Geophysical Research Atmospheres*, 117,
53 <https://doi.org/10.1029/2012JD018143>, 2012.

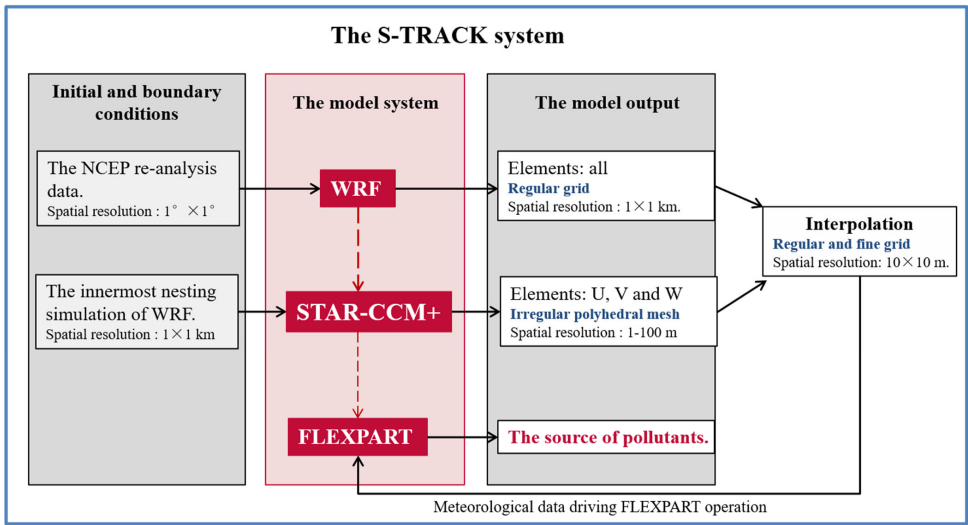
54 Stam, J.: Stable Fluids, *ACM Trans. Graph.*, 1999, <https://doi.org/10.1145/311535.311548>, 1999.

55 Steenburgh, W., J., Stoll, R., Gowardhan, A., Kochanski, A., K., Brown, and M., J.: One-Way Coupling of the WRF-QUIC
56 Urban Dispersion Modeling System, *Journal of Applied Meteorology and Climatology*, *J Appl Meteorol Climatol*,
57 <https://doi.org/10.1175/JAMC-D-15-0020.1>, 2015.

58 Stohl, A.: A backward modeling study of intercontinental pollution transport using aircraft measurements, *J. Geophys. Res.*,
59 108, 4370, <https://doi.org/10.1029/2002jd002862>, 2003.

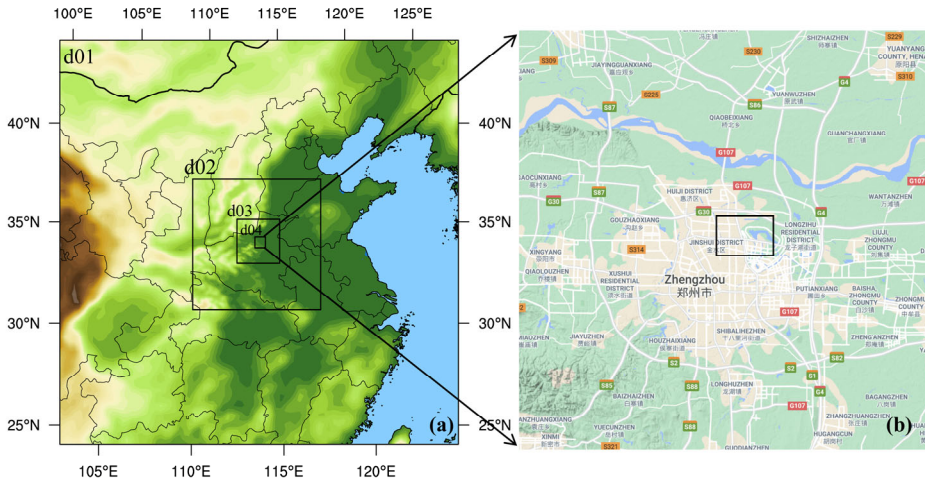
60 Stohl, A., and James, P.: A Lagrangian Analysis of the Atmospheric Branch of the Global Water Cycle. Part I: Method
61 Description, Validation, and Demonstration for the August 2002 Flooding in Central Europe, *J Hydrometeorol*, 5, 656,
62 [https://doi.org/10.1175/1525-7541\(2004\)0052.0.CO;2](https://doi.org/10.1175/1525-7541(2004)0052.0.CO;2), 2004.

1 Stohl, A., Forster, C., Frank, A., Seibert, P., and Wotawa, G.: Technical note: The Lagrangian particle dispersion model
2 FLEXPART version 6.2, *Atmos. Chem. Phys.*, 5, 2461-2474, <https://doi.org/10.5194/ACP-5-2461-2005>, 2005.
3 Stull, R. B.: *An Introduction to Boundary Layer Meteorology*, Springer Netherlands, Dordrecht., 1988.
4 Sui, L., Jiang, M., Li, Z., and Zhou, S.: Diffusion effect analysis of pollution gas under the impact of urban three-dimensional
5 pattern, in: 5th International Conference on Energy and Environmental Protection, Shengzhen, China, 17-18, September 2016,
6 903-909, 2016.
7 Temimi, M., Fonseca, R., Reddy, N. N., Weston, M., and Naqbi, H. A.: Assessing The Impact of Changes in Land Surface
8 Conditions on WRF Predictions in Arid Regions, *J Hydrometeorol*, 21, 2829-2853, <https://doi.org/10.1175/JHM-D-20-0083.1>,
9 2020.
10 Tewari, M., Kusaka, H., Chen, F., Coirier, W. J., Kim, S., Wyszogrodzki, A. A., and Warner, T. T.: Impact of coupling a
11 microscale computational fluid dynamics model with a mesoscale model on urban scale contaminant transport and dispersion,
12 *Atmos. Res.*, 96, 656-664, <https://doi.org/10.1016/j.atmosres.2010.01.006>, 2010.
13 Vogelezang, D., and Holtslag, A.: Evaluation and model impacts of alternative boundary-layer height formulations, *Bound-
14 Lay. Meteorol.*, 81, 245-269, <https://doi.org/10.1007/BF02430331>, 1996.
15 Yu, C., Zhao, T., Bai, Y., Zhang, L., Kong, S., Yu, X., He, J., Cui, C., Yang, J., You, Y., Ma, G., Wu, M., and Chang, J.:
16 Heavy air pollution with a unique “non-stagnant” atmospheric boundary layer in the Yangtze River middle basin aggravated
17 by regional transport of PM2.5 over China, *Atmos. Chem. Phys.*, 20, 7217-7230, <https://doi.org/10.5194/acp-20-7217-2020>,
18 2020.
19 Yu, T. Y.: Source identification of emission sources for hydrocarbon with backward trajectory model and statistical methods,
20 *Pol. J. Environ. Stud.*, 26(2), 893-902, <https://doi.org/10.15244/pjoes/65744>, 2017.
21 Yucong, Miao, Shuhua, Liu, Hui, Zheng, Yijia, Zheng, Bicheng, and Chen: A multi-scale urban atmospheric dispersion model
22 for emergency management, *Adv Atmos Sci*, 31, 13, <https://doi.org/10.1007/s00376-014-3254-9>, 2014.
23 Zhang, H., Xu, T., Zong, Y., Tang, H., Liu, X., and Wang, Y.: Influence of Meteorological Conditions on Pollutant Dispersion
24 in Street Canyon, *Procedia Engineering*, 121, 899-905, <https://doi.org/10.1016/J.PROENG.2015.09.047>, 2015.
25 Zhang, H., Tang, S., Yue, H., Wu, K., Zhu, Y., Liu, C.-J., Liang, B., and Li, C.: Comparison of Computational Fluid Dynamic
26 Simulation of a Stirred Tank with Polyhedral and Tetrahedral Meshes, *Iran. J. Chem. Chem. Eng.*, 39, 311-319,
27 <https://doi.org/10.30492/IJCCE.2019.34950>, 2020.
28 Zheng, Y., Miao, Y., Liu, S., Chen, B., Zheng, H., and Wang, S.: Simulating Flow and Dispersion by Using WRF-CFD
29 Coupled Model in a Built-Up Area of Shenyang, China, *Adv. Meteorol*, 2015, 1-15, <https://doi.org/10.1155/2015/528618>,
30 2015.
31



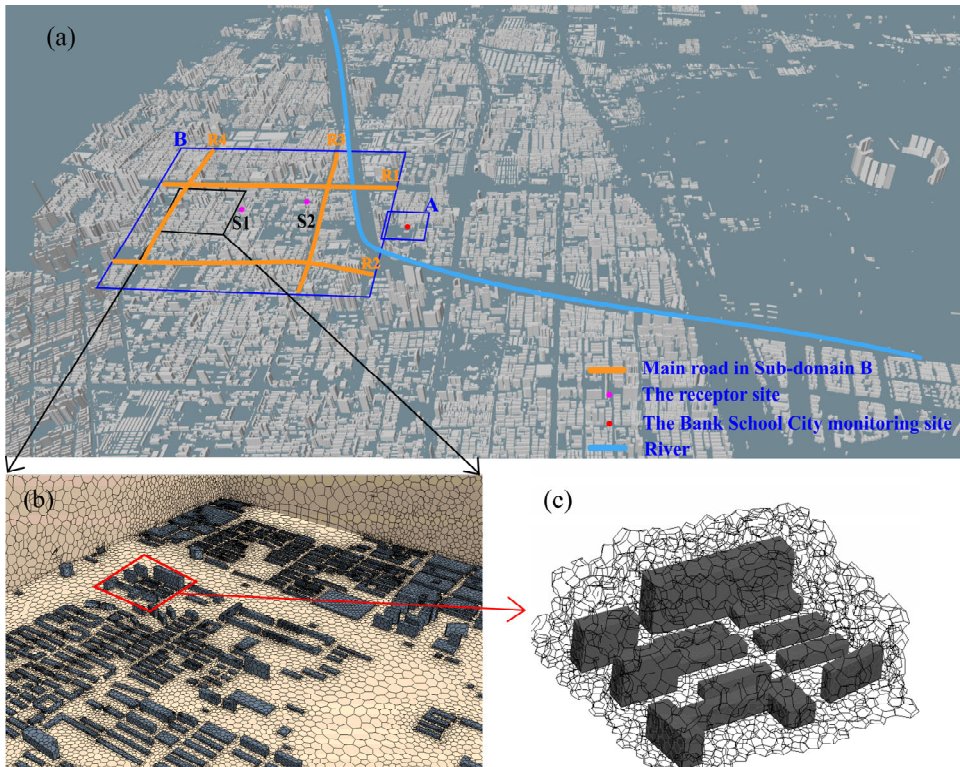
1
 2 **Figure 1: The S-TRACK system: The role of WRF, STAR-CCM+ and FLEXPART in the S-**
 3 **TRACK system and the process of gradual refinement of resolution.**

4



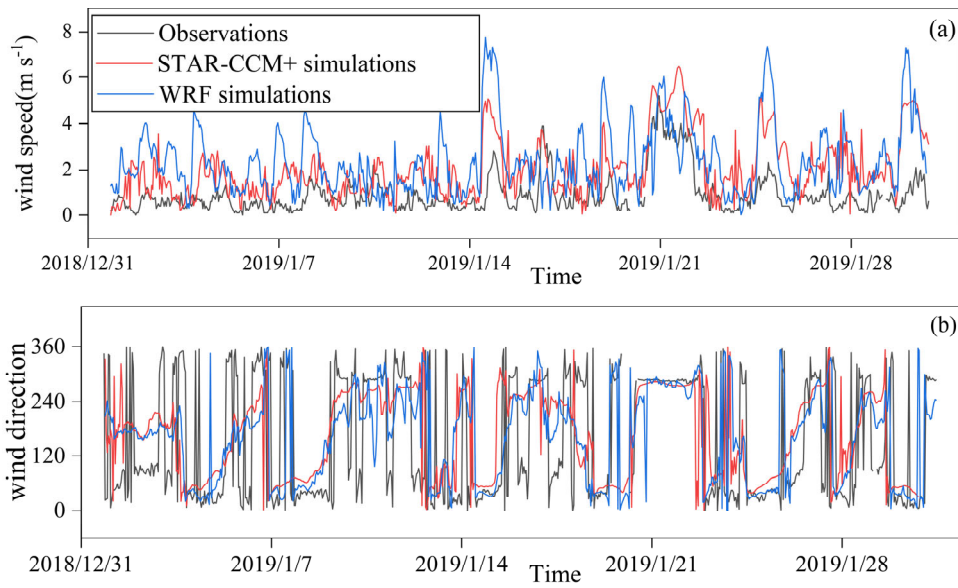
1
 2 **Figure 2: Domain configuration of the WRF model: (a) the range of the four nested domains (d1-**
 3 **d4); (b) the innermost nested domain (d4), within which the black box represents the STAR-CCM+**
 4 **simulation domain (extracted from © Google Maps 2021).**

5



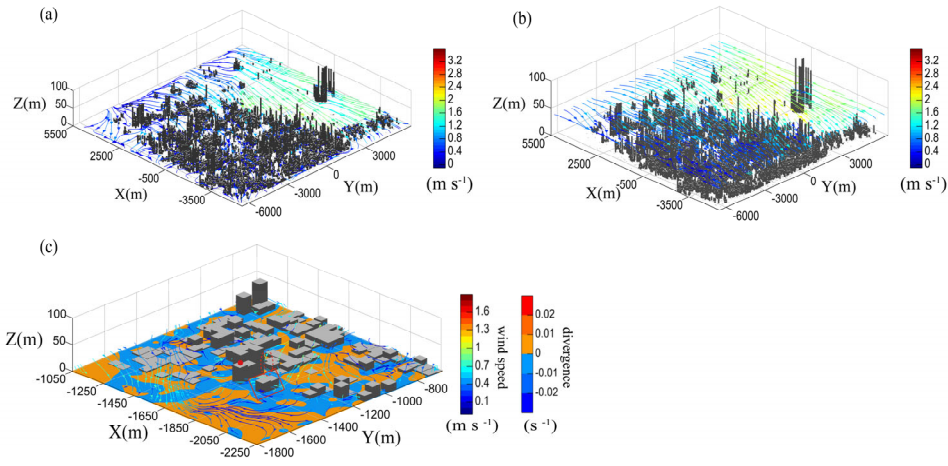
1
 2 **Figure 3: The computational domain of the STAR-CCM+ is shown in (a). The sub-domain A is used**
 3 **for detailed analysis of the wind environment, and the Bank School City (BSC) monitoring site**
 4 **marked with the red dot. Sub-domain B is used to analyse the potential impact**
 5 **contribution of traffic source on receptor sites in the region, with magenta dots (S1 and S2)**
 6 **indicating the receptor sites and Orange line indicating the main roads. The polyhedral mesh**
 7 **used to divide the STAR-CCM+ simulation area. The mesh details of the vertical cross section and**
 8 **building surface are shown in (b), and the 3D meshes are shown in (c).**

9



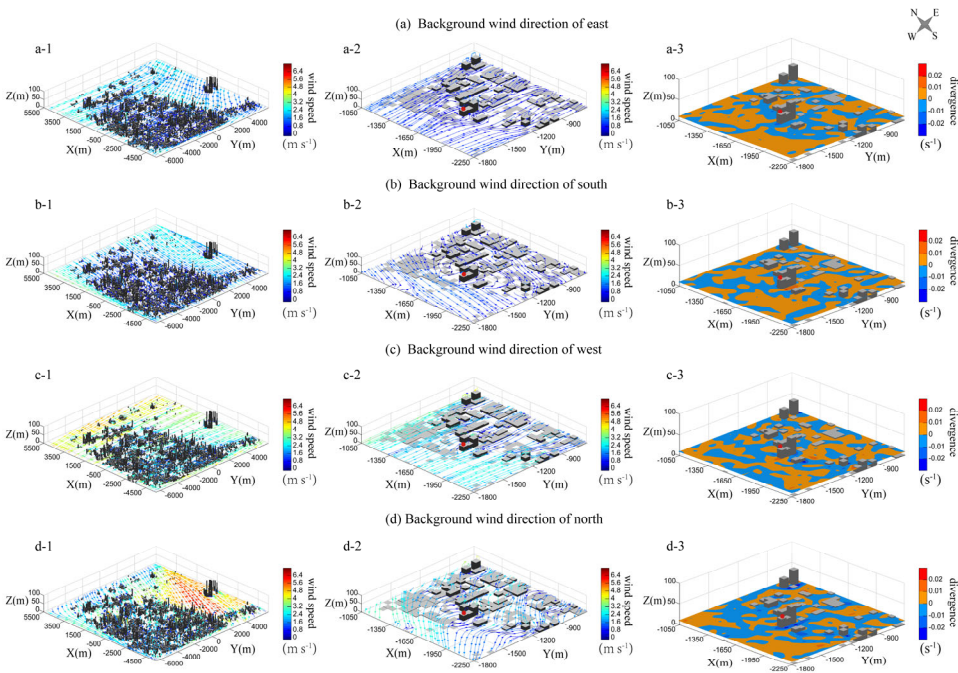
1
 2 **Figure 4: Evaluation of the wind simulation results at the BSC monitoring site (see in Fig. 3a): the**
 3 **simulated, by WRF (blue line) and STAR-CCM+ (red line) model, respectively, and the observed**
 4 **(grey line) hourly near-surface wind speeds (a) and wind directions (b).**

5



1
 2 **Figure 5: The simulated wind streamlines at the height of 5 m (a) and 40 m (b) averaged in January**
 3 **2019 in the whole S-TRACK simulation domain; the simulated wind streamlines and divergence (c)**
 4 **at the near-surface averaged in January 2019 in the sub-domain A (see in Fig. 3a). The BSC**
 5 **monitoring site is marked with red dot.**

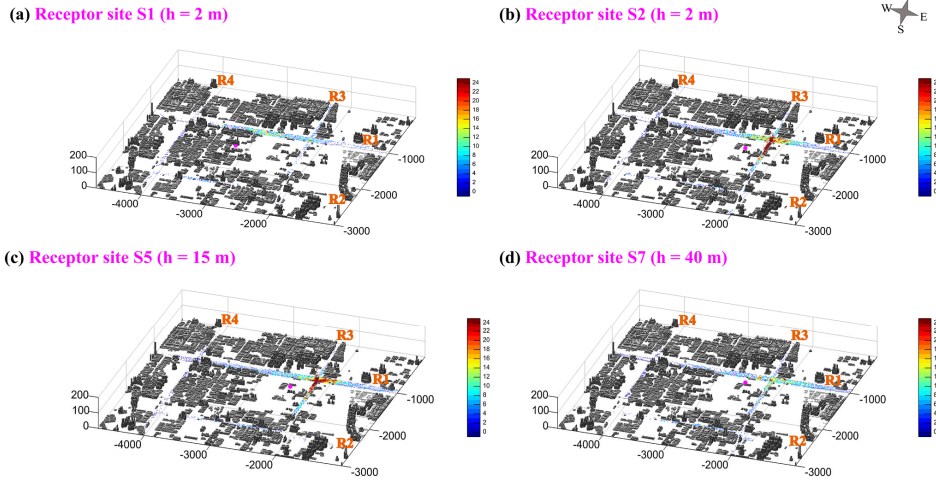
6



1
 2 **Figure 6: The wind field streamlines and divergences under the background wind directions of east**
 3 **(a), south (b), west (c) and north (d). The BSC monitoring site is marked with red dot.**

4

1

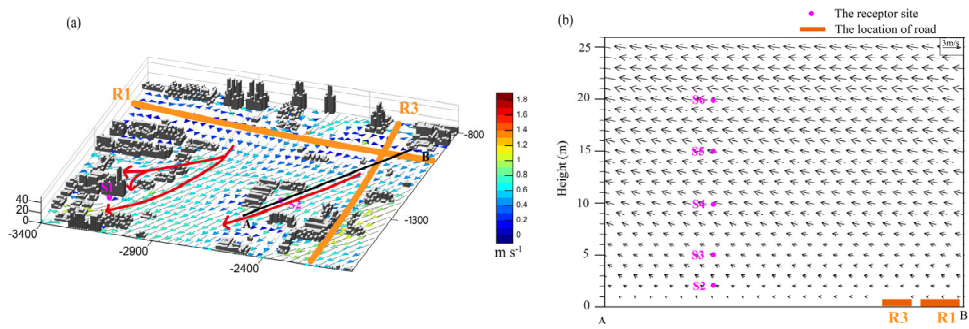


2

3 **Figure 7: Density distribution (refers to the number of particles that have stayed in the space of 10**
4 **m × 10 m in the horizontal direction and 5 m from the surface to above in the vertical direction) of**
5 **all trajectory points passing through the traffic roads that received from different receptor sites**
6 **(S1, S2, S5, and S7, see details in Table 4). The four receptor sites are all marked with magenta dots.**

7

1



2
3 **Figure 8:** The (a) average surface wind and (b) vertical structure of average winds that along the
4 wind direction around the receptor site S2 (line AB) in January 2019. The road R1 is marked with
5 orange line; the location of the vertical profile is shown in black line, and the receptor sites S1 to S6
6 are all marked with magenta dots.

7

8

1 **Table 1. The list of variables required to run FLEXPART and the sources of variables.**

variable	Description	Source
PB	base value of pressure	WRF
P	perturbation of pressure	WRF
PHB	base value of geopotential	WRF
PH	perturbation of geopotential	WRF
T	temperature	WRF
QVAPOR	specific humidity	WRF
MAPFAC_M	map factor	WRF
PSFC	surface pressure	STAR-CCM+
U10	10 m wind along x axis	STAR-CCM+
V10	10 m wind along y axis	STAR-CCM+
T2	2 m temperature	WRF
Q2	2 m dew point	WRF
SWDOWN	surface solar radiation (optional)	WRF
RAINNC	large scale precipitation (optional)	WRF
RAINC	convective precipitation (optional)	WRF
HFX	surface sensible heat flux (optional)	STAR-CCM+
U	wind along x axis	STAR-CCM+
V	wind along y axis	STAR-CCM+
W	Cartesian vertical velocity	STAR-CCM+

2
3 **Table 2 Parameterization scheme for the physical processes set up in the WRF model.**

Physical management	Parameterization	Reference
Microphysics scheme	Lin	Lin et al. (1983)
Longwave radiation scheme	RRTMG	Iacono et al. (2008)
Shortwave radiation scheme	RRTMG	Iacono et al. (2008)
Land surface scheme	Noah	Chen and Dudhia (2001)
Planetary boundary layer scheme	MYNN3	Nakanishi and Niino (2006)

4
5
6
7 **Table 3 Statistical performances of the hourly near-surface meteorology simulated by the WRF model.**

	R	MB	ME	RMSE
T	0.80	-1.86 (K)	2.33 (K)	2.82 (K)
RH	0.70	-5.95 (%)	11.5 (%)	15.0 (%)
P	0.98	3.66 (hPa)	3.66 (hPa)	3.77 (hPa)
WS	0.45	1.44 (m s ⁻¹)	1.58 (m s ⁻¹)	1.97 (m s ⁻¹)

8
9 **Table R4. Locations of receptor sites and the corresponding [potential contribution ratios PCR](#).**

Receptor site	Location (x, y, z)	potential contribution ratio PCR				
		R1	R2	R3	R4	All
S1	(-3200 m, -1420 m, 2 m)	1.81%	-	-	-	-
S2	(-2500 m, -1300 m, 2 m)	2.38%	0.18%	1.32%	0.16%	4.05%
S3	(-2500 m, -1300 m, 5 m)	2.57%	0.29%	1.28%	0.10%	4.25%
S4	(-2500 m, -1300 m, 10 m)	2.71%	0.32%	1.18%	0.12%	4.33%
S5	(-2500 m, -1300 m, 15 m)	2.98%	0.27%	1.22%	0.20%	4.67%
S6	(-2500 m, -1300 m, 20 m)	2.75%	0.37%	1.09%	0.17%	4.38%
S7	(-2500 m, -1300 m, 40 m)	2.30%	0.39%	0.70%	0.25%	3.64%
S8	(-2500 m, -1300 m, 50 m)	1.94%	0.57%	0.68%	0.36%	3.55%

1

2